Observation of orbital waves as elementary excitations in a solid

E. Saitoh*, S. Okamoto†, K. T. Takahashi*, K. Tobe*, K. Yamamoto*, T. Kimura*, S. Ishihara†§, S. Maekawa† & Y. Tokura*‡

** Department of Applied Physics, University of Tokyo, Tokyo 113-8656, Japan*
† Institute for Materials Research, Tohoku University, Sendai 980-8577, Japan
‡ Joint Research Center for Atom Technology (JRCAT) and Correlated Electron Research Center (CERC), Tsukuba 305-0046, Japan

A basic concept in solid-state physics is that when some kind of symmetry in a solid is spontaneously broken, collective excitations will arise[1]. For example, phonons are the collective excitations corresponding to lattice vibrations in a crystal, and magnons correspond to spin waves in a magnetically ordered compound. Modulations in the relative shape of the electronic clouds in an orbitally ordered state[2–9] could in principle give rise to orbital waves, or 'orbitons', but this type of elementary excitation has yet to be observed experimentally. Systems in which the electrons are strongly correlated—such as high-temperature superconductors and manganites exhibiting colossal magnetoresistivity—are promising candidates for supporting orbital waves, because they contain transition-metal ions in which the orbital degree of freedom is important[10,11]. Orbitally ordered states have been found in several transition-metal compounds[12,13], and orbitons have been predicted theoretically for $LaMnO_3$ (refs 4, 5). Here we report experimental evidence for orbitons in $LaMnO_3$, using Raman scattering measurements. We perform a model calculation of orbiton resonances which provides a good fit to the experimental data.

In the perovskite $LaMnO_3$, all of the Mn ions are trivalent with four electrons in 3*d* orbitals. Because of the crystal-field potential from surrounding oxygen ions and the strong Hund coupling, the electronic configuration of a Mn^{3+} is $t_{2g}^3 e_g^1$ (spin quantum number $S = 2$). Therefore, one electron occupies one of the doubly degenerate e_g orbitals, and the ion has both spin and orbital degrees of freedom[14–16]. This latter degree of freedom is spontaneously frozen by the real-space ordering of the e_g orbitals accompanied by a Jahn–Teller (JT) type lattice distortion of the MnO_6 octahedra[17]; as shown in the inset of Fig. 1a, the $d_{3x^2-r^2}$ and $d_{3y^2-r^2}$ orbitals for e_g electrons are alternately ordered in the *x*–*y* plane (so called C-type orbital ordering) below the orbital ordering temperature $T_{OO} \approx 780$ K (ref. 13). In addition, the spin ordering appears below $T_N \approx 140$ K (refs 18, 19) where spins are aligned ferromagnetically in the *x*–*y* plane, and antiferromagnetically in the *z* direction (so-called A-type antiferromagnetic (AF) ordering). We address here the elementary excitations in the orbitally ordered state of $LaMnO_3$.

To describe the orbital degree of freedom theoretically, we introduce the pseudo-spin **T** (quantum number $T = \frac{1}{2}$) which represents two possible choices of the occupied e_g orbital at a Mn ion. The quantum number $T_z = +(-)\frac{1}{2}$ corresponds to the state where the $d_{3z^2-r^2}(d_{x^2-y^2})$ orbital is occupied by an electron. In a solid, there are interactions between pseudo-spins at different ions which give rise to an orbital order–disorder phase transition[20]. In the orbitally ordered state, a macroscopic classical variable caused by the pseudo-spin—that is, the orbital order parameter—becomes finite. The order parameter in orbitally ordered $LaMnO_3$ is identified as $\mathbf{M}(\mathbf{k}) = (1/N)\Sigma_i e^{i\mathbf{k}\cdot\mathbf{r}_i}\langle \mathbf{T}_i \rangle = ((\sqrt{3}/4)\delta_{\mathbf{k}=(\pi\pi 0)}, 0, -(1/4)\delta_{\mathbf{k}=(000)})$, where $\langle \ldots \rangle$ indicates the thermal average, $\mathbf{r}_i$ is a position of the *i*th Mn ion and *N* is the number of ions. Consider the excitations of the orbital sector in the orbitally ordered state. Such an excitation corresponds to a change of the occupied orbital, that is, to a change in the shape of the electron cloud. This is represented by a deviation of $\mathbf{T}_i$ from $\langle \mathbf{T}_i \rangle$.

Once the orbital excitation occurs at a site, it propagates in a solid through the interactions between orbitals at different ions, as does the spin excitation in a magnetically ordered state. This collective excitation and its quantized object are termed 'orbital wave' and 'orbiton' respectively. A schematic illustration is presented in Fig. 1b. The energy, dispersion and symmetry of the orbital wave are calculated from a model describing the interactions between orbitals. Here, considering the fact that $LaMnO_3$ is a Mott insulator and that the Hund coupling in a Mn ion is strong, the important interaction between orbitals is caused by the exchange of electrons between Mn ions. The model hamiltonian is[4,5,16]:

$$H = -2\sum_{(ij)}\left\{J_1 K_1\left(\frac{1}{4} - \tau_i^l \tau_j^l\right) + J_2 K_2\left(\frac{3}{4} + \tau_i^l \tau_j^l + \tau_i^l + \tau_j^l\right)\right\} \quad (1)$$

where $\tau_i^l = \cos(2\pi m_l/3)T_{iz} - \sin(2\pi m_l/3)T_{ix}$ with $(m_x, m_y, m_z) = (1, 2, 3)$, and where *l* denotes the direction of a bond connecting a site *i* and its nearest neighbouring site *j*. The quantities $K_1 = 1/4 - \mathbf{S}_i \cdot \mathbf{S}_j$ and $K_2 = 3/4 + \mathbf{S}_i \cdot \mathbf{S}_j$ involve $\mathbf{S}_i$ the spin operator

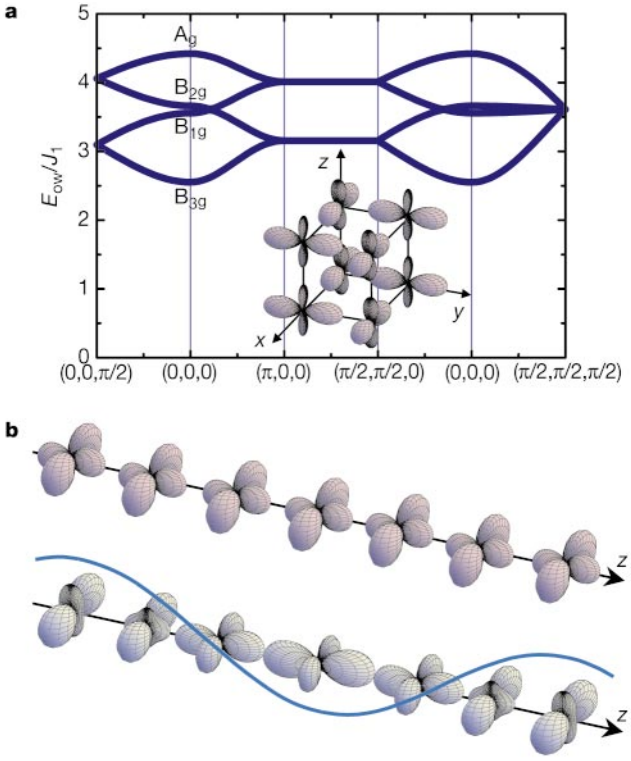

Figure 1 Dispersion relation and schematic illustration of an orbital wave. **a**, Theoretical results for the dispersion relation of the orbital wave in the C-type orbitally ordered state with the A-type AF structure (see text). The parameter values in equation (1) are chosen to be $J_2/J_1 = 0.35$. E_{OW} denotes energy of the orbital wave. In addition to the hamiltonian, equation (1), the interaction between the pseudo-spin $\mathbf{T}_i$ and the static Jahn–Teller-type lattice distortion in a MnO_6 octahedron is introduced. This is described by the hamiltonian $H_{JT} = g\Sigma_i(Q_{i3}T_{iz} + Q_{i2}T_{ix})$, where Q_{i2} and Q_{i3} are the two normal coordinates of the displacements of the O ions surrounding a Mn ion at site *i*, and *g* is a coupling constant. We choose $(1/N)\Sigma_i e^{i\mathbf{k}\mathbf{r}_i}(Q_{i2}, Q_{i3}) = Q((\sqrt{3}/2)\delta_{\mathbf{k}=(\pi\pi 0)}, -\frac{1}{2}\delta_{\mathbf{k}=(000)})$ and $gQ/J_1 = 0.7$. This interaction adds an energy $(0.8gQ)$ to the centre of gravity of the dispersion relation. The Brillouin zone for the tetragonal lattice with the D_{4h} symmetry is adopted. A schematic picture of the orbitally ordered state (electron cloud) in $LaMnO_3$ is shown in the inset. **b**, Schematic illustration of the orbital wave. Top, the electron cloud in the ground state. Bottom, a snapshot of the electron cloud when an orbital wave is excited. The wavevector of the orbital wave is chosen to be $(0, 0, 6\pi/a)$, with *a* being the bond length between the nearest neighbouring Mn ions.

§ Present address: Department of Applied Physics, University of Tokyo, Tokyo 113-8656, Japan.

with spin quantum number $S = 1/2$. Two terms in H correspond to the different exchange processes and (J_1, J_2) are amplitudes of these interactions. It has been shown[4,5] that this model can well describe the actual situation of the spin and orbital states in $LaMnO_3$. The exchange of virtual phonons also causes the interaction between orbitals. As it is estimated to be smaller than J_1 and has a similar form to equation (1), this contribution is included in the parameter J_1K_1 of the equation.

The dispersion relation is calculated by applying the Holstein–Primakoff theory to equation (1) for the hypothetical tetragonal (D_{4h}) lattice of $LaMnO_3$, and is presented in Fig. 1a. We assume that spin and lattice are frozen, as their dynamics are expected to be slower than that of the orbitals in $LaMnO_3$. Then, the effect of the static JT-type lattice distortion in a MnO_6 octahedron is introduced, which adds some energy to the centre of gravity of the orbiton dispersion described by equation (1). At the Γ point, the four modes of the orbital wave have A_g, B_{2g}, B_{1g} and B_{3g} symmetries of the D_{4h} group. The band width of the orbital wave is of the order of the exchange interactions $J_{1(2)}$. A gap of the order of the band width is opened due to the anisotropy in the interactions between pseudo-spins.

Raman scattering has been used to identify the orbital waves at the Γ point. We have measured the Raman scattering spectra for a detwinned single crystal of $LaMnO_3$. The detwinned crystal enables us to investigate the detailed polarization dependence. Raman scattering measurements were performed using a microscope spectroscopy system in the nearly backscattering configuration. The 514.5-nm line (2.4 eV) of an Ar^+ laser was used for excitation, and the laser power at the focus spot (~5 μm in diameter) was kept below 1 mW. The excitation energy corresponds to the energy scale of the charge-transfer interaction between the O 2*p* and the Mn 3*d* orbitals[21,22]. The polarization configuration of the incident and the scattered light is represented by (x, y) and so on. As illustrated in the inset of Fig. 1a, x, y and z are taken to be the directions of Mn–Mn bonds and $x + y = x'$ ($x - y = y'$). Spectra were measured in six polarization configurations: (x, x), (x, y), (x', x'), (x', y'), (z, z) and (z, x).

In Figs 2a and b, we display the Raman scattering spectra at 9 K (the orbitally ordered ground state) in four polarization configurations for the $LaMnO_3$ single crystal. We first discuss briefly phonon modes activated by the JT lattice distortions. Peak structures observed in a lower-energy region (≲100 meV) can be assigned to phonon scattering, as discussed previously[23]. Among them, two intense modes can be observed in the (x, x) polarization spectrum at 60 and 75 meV, and another mode for the (z, z) polarization at 60 meV. These modes have been identified as the activated oxygen modes due to a cooperative JT distortion[24]. Figure 2c shows the temperature variation of these phonon modes in the (x, x) polarization spectrum. With an increase in temperature, the spectral intensity decreases and then almost disappears near the structural phase transition at $T_{JT} \approx 750$ K (ref. 17). The observed temperature dependence of these phonon peaks confirms that these modes reflect the order parameter of the JT lattice distortion.

The most notable feature in the present Raman study is found in a higher-energy region (≳100 meV). In the (x, x) configuration spectrum at 9 K (Fig. 2a), three characteristic broad peak structures are observed at 125, 145 and 160 meV. One broad peak is also observed at 160 meV in the (z, z) configuration (Fig. 2b). The peak features in the energy region above ~100 meV show strong polarization dependence, which is displayed in Figs 3a–c. The high-energy Raman bands become weak with increasing temperature, and almost disappear around T_{OO} (Fig. 2d). This temperature profile parallels that of the phonon modes in the lower-energy region.

Raman bands for transition-metal oxides at such a high-energy scale are usually assigned to multi-phonon scattering. However, these Raman bands in the present compound cannot be attributed to simple multi-phonon scattering for the following reasons. (1) The Raman-shift energy of the high-energy Raman bands cannot be reproduced by any combination of the observed Raman and infrared phonon modes. For comparison, we plot in Figs 2a and b the (x, x) and (z, z) spectra, respectively, as a function of doubled Raman shift (blue lines). Although the multi-phonon Raman scattering energy may shift from the sum of the one-

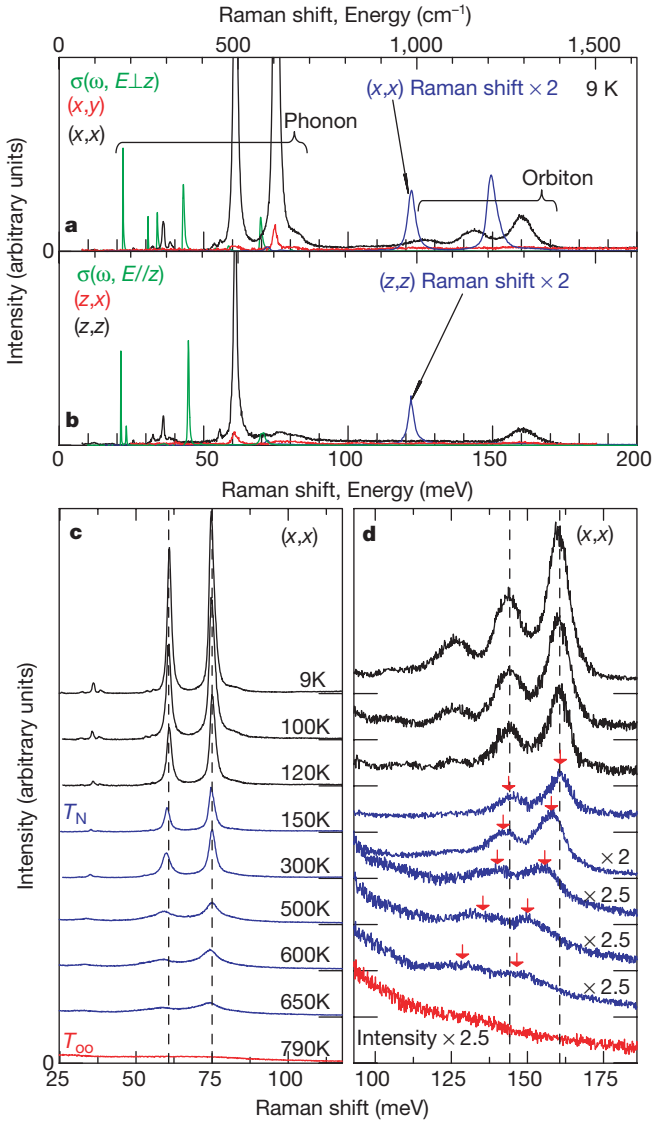

Figure 2 Experimental results for Raman scattering spectra of a detwinned $LaMnO_3$ crystal. **a**, **b**, Raman scattering spectra with four polarization configurations (black and red lines) and optical conductivity spectra (σ) (green lines) at 9 K. The crystal was obtained by the floating-zone method and a post-annealing procedure. The post-annealing was performed under an oxygen partial pressure of 3×10^{-4} atm and at a cooling rate of ~10 K h^{-1}. To see the possible components of two-phonon excitations, we plot the (x, x) and (z, z) spectra as functions of the double Raman shift (blue lines). **c**, **d**, Temperature variation of Raman scattering spectra in the (x, x) configuration for the $LaMnO_3$ crystal. In **d**, the vertical axis (intensity) of the spectra above 300 K is stretched by a factor of 2 (300 K) or 2.5 (500–790 K). Black dashed lines are located at the peak positions of the respective Raman bands at 9 K. Although the peak positions of the phonon modes are almost independent of temperature (**c**), those of the Raman bands at higher energy (red arrows) shift appreciably with temperature above $T_N \approx 140$ K (**d**). This anomaly in the high-energy Raman band around T_N signals the close connection of the orbiton state to the magnetic ordering, as expected from the original effective hamiltonian equation (1), and/or reflects the related change of the orbital order parameter[13].

phonon energy to a limited extent due to the nonlinearity of lattice dynamics, such an effect cannot increase the multi-phonon energy. (We note that a weak phonon band has been reported around 650 cm^{-1} in previous studies on Raman spectra for $LaMnO_{3+\delta}$ (refs 25, 26). Such a phonon band is much weaker in the present Raman spectra, see Fig. 2a, but tends to grow with increasing oxygen contents or slightly doped Sr contents ($x \sim 0.06$) in $La_{1-x}Sr_xMnO_3$ where the high-energy Raman bands are rather suppressed.) (2) A substantial temperature-dependent energy shift of the peaks (up to 10 meV) is observed, in contrast to a negligible dependence of the observed phonon mode energies (see and compare Fig. 2d and c). (3) We also measured the spectra for $RMnO_3$ (where R is Nd or Gd). The decrease of the ionic radius of the R-site causes the suppression of the intensity of the phonon modes, but does not suppress that of the high-energy Raman bands. For these reasons, the observed Raman bands (for example, that at 160 meV) cannot be attributed to simple multi-phonon scattering. Charge excitations cannot be responsible for these Raman bands, because of the large charge gap energy (~1 eV) in the ground state of $LaMnO_3$ (ref. 22). As for the two-magnon scattering, the A-type AF ordering (in-plane ferromagnetic) prohibits all the magnon scattering except for the (z, z) component.

The above unconventional high-energy excitations in the Raman scattering experiments are best interpreted in terms of the theoretical calculations of the orbital wave. The second-order interaction between electrons and photons creates an orbiton through the exchange of electrons. Consider a pair of the nearest neighbouring O and Mn ions in orbitally ordered $LaMnO_3$. The incident photon excites an electron from the O $2p$ orbital to an unoccupied Mn e_g orbital. Via a second photon interaction, one of the two e_g electrons returns to the O ion. In the final scattering state, the orbital occupation of the Mn ion is changed, that is, a single orbiton is created by this two-photon process. The photon-induced exchange of electrons between the nearest neighbouring Mn ions also excites orbitons[27]. Both cross-sections for Raman scattering are estimated to be of the same order of magnitude as the two-magnon process in antiferromagnets. Electronic excitations between the crystal-field levels have been examined by Raman spectroscopy for $4f$ electron systems[28], where the local orbital excitations occur through the electronic transitions on a rare-earth ion. However, this is unlike the present case, showing the **k**-dispersion of the orbital excitation on the almost degenerate crystal-field levels.

We have calculated the Raman scattering spectra for several configurations of light polarization (Fig. 3d–f), and compared them with the experimental results (Fig. 3a–c). The actual small lattice distortions with monoclinic symmetry are taken into account[29]. The peaks labelled A and B correspond to creation of single orbitons with A_g and B_{1g} symmetry (Fig. 1a) respectively. Peak C corresponds to the excitation at $\mathbf{k} = (\pi 00)$ in Fig. 1a, and becomes Raman active due to the monoclinic lattice distortion. (We estimate J_1 to be about 50 meV, from the analyses of the experimental spin wave spectrum in $LaMnO_3$ (ref. 30).) The theoretical results are in qualitatively good agreement with experiment. The following characteristics of the spectra provide strong evidence that the observed peaks originate from orbitons. (1) The strongest intensity of peak A for the (x, x) and (x', x') configurations originates from an interference effect in the in-phase A_g mode. (2) The weak peak C for the (x, x) and (x', x') configurations appears due to the small lattice distortion, as mentioned above. (3) The spectra for the (x, y) and (z, x) configurations are much weaker because, in the excitation process introduced above, an orbiton is not created for these configurations.

We expect that the present systematic theoretical and experimental studies of orbital waves and their quantized equivalents, orbitons, will also help us to understand better the thermal, electrical and magnetic properties of orbitally ordered systems. These properties are all strongly affected by the nature of the orbital state. It is certainly worthwhile to search for such orbital waves in other transition-metal compounds with orbital ordering, in order to ensure the general nature of this concept. □

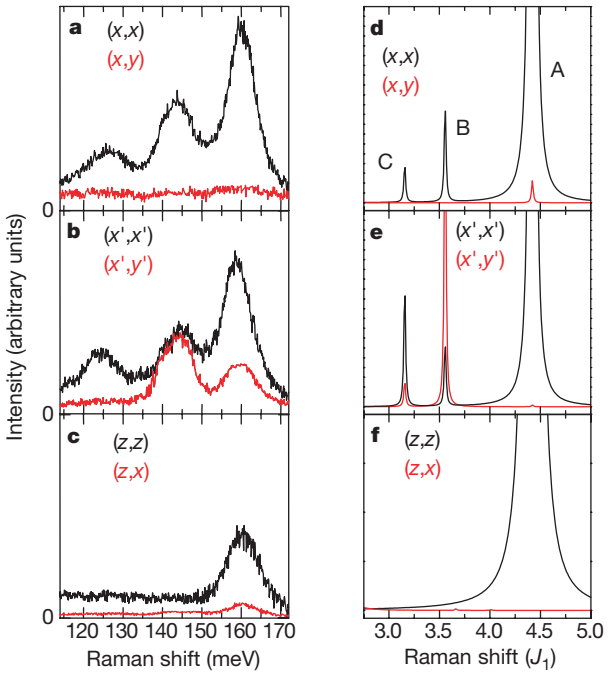

Figure 3 Comparison between the experimental and theoretical Raman scattering spectra for $LaMnO_3$. **a**–**c**, Experimental Raman scattering spectra in several polarization configurations for a detwinned single crystal of $LaMnO_3$ at 9 K between 110 and 175 meV. **d**–**f**, Theoretical Raman scattering spectra due to orbitons in the C-type orbitally ordered state with the A-type AF structure. The displacements of the O ions observed in the monoclinic phase of $LaMnO_3$ are introduced in the calculation. J_1 is estimated to be about 50 meV from the analyses of the experimental spin wave spectrum in $LaMnO_3$.

Received 9 November 2000; accepted 8 January 2001.

1. Anderson, P. W. *Basic Notions of Condensed Matter Physics* (Benjamin-Cummings, London, 1984).
2. Cyrot, M. & Lyon-Caen, C. Orbital superlattice in the degenerate Hubbard model. *J. Phys. (Paris)* **36,** 253–266 (1975).
3. Komarov, A. G., Korovin, L. I. & Kudinov, E. K. Elementary excitation in systems with 'frozen' spin. *Sov. Phys. Solid State* **17,** 1531–1533 (1976).
4. Ishihara, S., Inoue, J. & Maekawa, S. Electronic structure and effective Hamiltonian in perovskite Mn oxides. *Physica C* **263,** 130–133 (1996).
5. Ishihara, S., Inoue, J. & Maekawa, S. Effective Hamiltonian in manganites: Study of the orbital and spin structures. *Phys. Rev. B* **55,** 8280–8286 (1997).
6. Khaliullin, G. & Oudovenko, V. Spin and orbital excitation spectrum in the Kugel-Khomskii model. *Phys. Rev. B* **56,** R14243–R14246 (1997).
7. Feiner, L. F., Oleś, A. M. & Zaanen, J. Quantum disorder versus order-out-of-disorder in the Kugel-Khomskii model. *J. Phys. Condens. Matter* **10,** L555–L561 (1998).
8. van den Brink, J., Stekelenburg, W., Khomskii, D. I., Sawatzky, G. A. & Kugel, K. I. Elementary excitations in the coupled spin-orbit model. *Phys. Rev. B* **58,** 10276–10282 (1998).
9. Perebeinos, V. & Allen, P. B. Toward a theory of orbiton dispersion in $LaMnO_3$. *Phys. Status Solidi B* **215,** 607–615 (1999).
10. Tokura, Y. & Nagaosa, N. Orbital physics in transition-metal oxides. *Science* **288,** 462–468 (2000).
11. Imada, M., Fujimori, A. & Tokura, Y. Metal-insulator transitions. *Rev. Mod. Phys.* **70,** 1039–1263 (1998).
12. Ito, Y. & Akimitsu, J. Observation of orbital ordering in K_2CuF_4. *J. Phys. Soc. Jpn* **40,** 1333–1338 (1976).
13. Murakami, Y. *et al.* Resonant x-ray scattering from orbital ordering in $LaMnO_3$. *Phys. Rev. Lett.* **81,** 582–585 (1998).
14. Goodenough, J. B. Theory of the role of covalence in the perovskite-type manganites [La, M(II)]MnO_3. *Phys. Rev.* **100,** 564–573 (1955).
15. Kanamori, J. Superexchange interaction and symmetry properties of electron orbitals. *J. Phys. Chem. Solids* **10,** 87–98 (1959).
16. Kugel, K. I. & Khomskii, D. I. Crystal structure and magnetic properties of substances with orbital degeneracy. *Sov. Phys. JETP* **37,** 725–730 (1973).
17. Rodriguez-Carvajal, J., Hennion, M., Moussa, F. & Moudden, A. H. Neutron diffraction study of the Jahn-Teller transition in stoichiometric $LaMnO_3$. *Phys. Rev. B* **57,** R3189–R3192 (1998).
18. Wollan, E. O. & Koehler, W. C. Neutron diffraction study of the magnetic properties of the series of perovskite-type compounds [(1–x)La, xCa]MnO_3. *Phys. Rev.* **100,** 545–563 (1955).
19. Matsumoto, G. Study of $(La_{1-x}Ca_x)MnO_3$. I. Magnetic structure of $LaMnO_3$. *J. Phys. Soc. Jpn* **29,** 606–615 (1970).

20. Kaplan, M. D. & Vekhter, B. G. *Cooperative Phenomena in Jahn-Teller Crystals* (Plenum, New York, 1995).
21. Saitoh, T. *et al.* Electronic structure of $La_{1-x}Sr_xMnO_3$ studied by photoemission and x-ray absorption spectroscopy. *Phys. Rev. B* **51,** 13942–13951 (1995).
22. Arima, T. & Tokura, Y. Optical study of electronic structure in perovskite-type RMO_3 (R = LaY; M = Sc, Ti, V, Cr, Mn, Fe, Co, Ni, Cu). *J. Phys. Soc. Jpn* **64,** 2488–2501 (1995).
23. Iliev, M. N. *et al.* Raman spectroscopy of orthorhombic perovskite $YMnO_3$ and $LaMnO_3$. *Phys. Rev. B* **57,** 2872–2877 (1998).
24. Yamamoto, K., Kimura, T., Ishikawa, T., Katsufuji, T. & Tokura, Y. Raman spectroscopy of the charge-orbital ordering in layered manganites. *Phys. Rev. B* **61,** 14706–14715 (2000).
25. Podobedov, V. B., Weber, A., Romero, D. B., Rice, J. P. & Drew, H. D. Effect of structural and magnetic transitions in $La_{1-x}M_xMnO_3$ (M = Sr, Ca) single crystals in Raman scattering. *Phys. Rev. B* **58,** 43–46 (1998).
26. Abrashev, M. V. *et al.* Comparative study of optical phonons in the rhombohedrally distorted perovskites $LaAlO_3$ and $LaMnO_3$. *Phys. Rev. B* **59,** 4146–4153 (1999).
27. Inoue, J. *et al.* Raman scattering by orbital waves in perovskite $LaMnO_3$. *Physica B* **237–238,** 51–53 (1997).
28. Schaack, G. in *Light Scattering in Solids VII* (eds Cardona, M. & Güntherodt, G.) 24–173 (Springer, Berlin, 2000).
29. Mitchell, J. F. *et al.* Structural phase diagram of $La_{1-x}Sr_xMnO_{3+\delta}$: Relationship to magnetic and transport properties. *Phys. Rev. B* **54,** 6172–6183 (1996).
30. Hirota, K., Kaneko, N., Nishizawa, A. & Endoh, Y. Two-dimensional planar ferromagnetic coupling in $LaMnO_3$. *J. Phys. Soc. Jpn* **65,** 3736–3739 (1996).

Acknowledgements

We thank N. Nagaosa, T. Katsufuji, P. Prelovšek and S. E. Barnes for discussions. This work was supported in part by NEDO Japan, CREST Japan, the Science and Technology Special Coordination Fund for Promoting Science and Technology, and Grant-in-Aid for Scientific Research Priority Area from the Ministry of Education, Science and Culture of Japan. S.O. acknowledges the financial support of JSPS. Part of the numerical calculation was performed in the supercomputing facilities in IMR, Tohoku University.

Correspondence and requests for materials should be addressed to Y.T. (e-mail: tokura@ap.t.u-tokyo.ac.jp).

Coherent branched flow in a two-dimensional electron gas

M. A. Topinka*, B. J. LeRoy†, R. M. Westervelt*†, S. E. J. Shaw†, R. Fleischmann‡, E. J. Heller†§, K. D. Maranowski‖ & A. C. Gossard‖

* *Division of Engineering and Applied Sciences,* † *Department of Physics,* § *Department of Chemistry and Chemical Biology, Harvard University, Cambridge, Massachusetts 02138, USA*
‡ *Max-Planck-Institut für Strömungsforschung, Bunsenstraße 10, D-37073 Göttingen, Germany*
‖ *Materials Department, University of California, Santa Barbara, California 93106, USA*

Semiconductor nanostructures based on two-dimensional electron gases (2DEGs) could form the basis of future devices for sensing, information processing and quantum computation. Although electron transport in 2DEG nanostructures has been well studied, and many remarkable phenomena have already been discovered (for example, weak localization, quantum chaos, universal conductance fluctuations[1,2]), fundamental aspects of the electron flow through these structures have so far not been clarified. However, it has recently become possible to image current directly through 2DEG devices using scanning probe microscope techniques[3–13]. Here, we use such a technique to observe electron flow through a narrow constriction in a 2DEG—a quantum point contact. The images show that the electron flow from the point contact forms narrow, branching strands instead of smoothly spreading fans. Our theoretical study of this flow indicates that this branching of current flux is due to focusing of the electron paths by ripples in the background potential. The strands are decorated by interference fringes separated by half the Fermi wavelength, indicating the persistence of quantum mechanical phase coherence in the electron flow. These findings may have important implications for a better understanding of electron transport in 2DEGs and for the design of future nanostructure devices.

Images of electron flow from the quantum point contact (QPC) are obtained by raster scanning a negatively charged scanning probe microscope (SPM) tip above the surface of the device and simultaneously measuring the position-dependent conductance of the device. The negatively charged tip capacitively couples to the 2DEG, creating a depletion region that backscatters electron waves. When the tip is positioned over areas with high electron flow from the QPC, the conductance is decreased, whereas when the tip is over areas of relatively low electron flow the conductance is unmodified. By raster scanning the tip over the sample, a two-dimensional image of electron flow can be obtained.

The QPC sample is mounted in an atomic force microscope and cooled to liquid He temperatures. The QPC is formed in the 2DEG inside a GaAs/AlGaAs heterostructure by negatively biasing two gates on the surface—a negative potential on these gates creates two depletion regions that define a variable-width channel between them, as shown in Fig. 1a. The heterostructure for the devices used in this experiment was grown by molecular beam epitaxy on an n-type GaAs substrate. The 2DEG resides 57 nm below the surface with mobility $\mu = 1.0 \times 10^6\,cm^2\,V^{-1}\,s^{-1}$ and density $n = 4.5 \times 10^{11}\,cm^{-2}$. These values of mobility and density correspond to a mean free path $l = 11\,\mu m$, Fermi wavelength $\lambda_F = 37$ nm, and

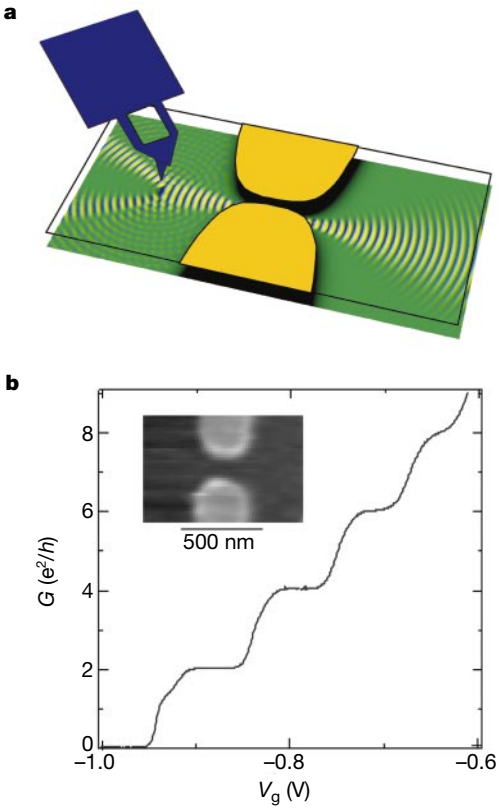

Figure 1 Experimental set-up. **a**, Schematic diagram of the experimental set-up used for imaging electron flow. The tip introduces a movable depletion region which scatters electron waves flowing from the quantum point contact (QPC). An image of electron flow is obtained by measuring the effect the tip has on QPC conductance as a function of tip position. Two ohmic contacts ~1 mm away from the QPC (not shown) allow the conductance of the QPC to be measured using an a.c. lock-in amplifier at 11 kHz. The root-mean-square voltage across the QPC, 0.2 mV, was chosen in order not to heat electrons significantly above the lattice temperature of 1.7 K. **b**, Conductance of the QPC used for Fig. 2b versus QPC width controlled by the gate voltage. Steps at integer multiples of $2e^2/h$ are clearly visible. The inset is a topographic AFM image of the QPC.